solar

Article

Investigation of the Thermal Stability of a Solar Absorber Processed through a Hydrothermal Technique

S. A. Abdullahi [1,2,3,*], R. Akoba [1,2,4,5], J. Sackey [1,2], S. Khamlich [6,7], S. Halindintwali [8], Z. Y. Nuru [1,2,9] and M. Maaza [1,2]

1. UNESCO-UNISA Africa Chair in Nanosciences-Nanotechnology, College of Graduate Studies, University of South Africa, Muckleneuk Ridge, Pretoria P.O. Box 392, South Africa
2. Nanoscience's African Network (NANOAFNET), iThemba LABS-National Research Foundation, 1 Old Faure Road, P.O. Box 722, Somerset West, Cape Town 7129, South Africa
3. School of Preliminary Studies (SPS) Science, Physics Unit, Ibrahim Badamasi Babangida University, Lapai P.M.B 11, Niger State, Nigeria
4. Department of Physics, Busitema University, Tororo P.O. Box 236, Uganda
5. Department of Physics, Islamic University in Uganda, Mbale P.O. Box 2555, Uganda
6. Department of Mechanical Engineering, Cape Peninsula University of Technology, P.O. Box 1906, Bellville 7535, South Africa
7. Nanoenergy for Sustainable Development in Africa (NESDAF), P.O. Box 362, Western Cape 7139, South Africa
8. Department of Physics, Faculty of Natural Science, University of the Western Cape, Private Bag X 17, Bellville 7535, South Africa
9. Future Leader-African Independent Researcher, College of Natural and Computational Science, Physics, Adigra University, Adigrat P.O. Box 50, Ethiopia

* Correspondence: 66762588@mylife.unisa.ac.za or sabaa9175@gmail.com; Tel.: +27-657207059 or +234-8030776288

Citation: Abdullahi, S.A.; Akoba, R.; Sackey, J.; Khamlich, S.; Halindintwali, S.; Nuru, Z.Y.; Maaza, M. Investigation of the Thermal Stability of a Solar Absorber Processed through a Hydrothermal Technique. *Solar* **2022**, *2*, 414–431. https://doi.org/10.3390/solar2040025

Academic Editors: Jürgen Heinz Werner and Pedro Dinis Gaspar

Received: 23 May 2022
Accepted: 5 July 2022
Published: 28 September 2022

Abstract: In this work, we study the thermal stability of a hydrothermally treated stainless steel (SS) selective solar absorber by annealing in air in a temperature range between 300 °C and 700 °C for a soaking time of 2 h. Thermal stability testing in the presence of air is critical if the vacuum is breached. Therefore, the SS was characterized by X-ray diffraction (XRD), mechanical, and optical techniques. The XRD analysis shows that the grain size of the as-treated absorber is 67 nm, whereas those of the annealed absorbers were found to be in the range between 66 and 38 nm. The phase of the as-treated and annealed SS was further identified by XRD as Fe_2O_3. The EDS result shows that the elemental components of the SS were C, Cr, Fe, and O. The strain (ε) and stress (σ) calculated for the as-treated absorber are 1.2×10^{-1} and −2.9 GPa, whereas the annealed absorbers are found in the range of 4.4×10^{-1} to 5.2×10^{-1} and −121.6 to −103.2 GPa, respectively, at 300–700 °C. The as-treated SS absorbers exhibit a good spectra selectivity of 0.938/0.431 = 2.176, which compares with 0.941/0.403 = 2.335 after being annealed at 300 °C and 0.884/0.179 = 4.939 after being annealed at 700 °C. These results indicate a small improvement in absorptivity (0.941) and emissivity (0.403) after annealing at 300 °C, followed by a significant decrease after annealing at 700 °C. The obtained analysis confirms that the annealed SS absorber exhibits excellent selectivity and is suitable to withstand any thermal condition (≤700 °C) in air. Thus, using a cost-effective approach as demonstrated in this study, the as-treated and annealed SS absorber could be used for photo-thermal conversion applications.

Keywords: solar absorber; stainless-steel; absorptance; emittance; thermal stability; selectivity

1. Introduction

As a result of the global awareness of greenhouse gas emissions, air pollution, and energy security issues, many governments and researchers around the world have been motivated to search for alternative energies that must be environmentally friendly, clean, affordable, and sustainable [1]. Seeking an ecofriendly, cost-effective, and feasible alternative to overcome the energy crisis is one of the most significant challenges humanity faces today [2]. Solar energy is one of the attractive solutions to replace fossil fuels, among other diverse alternative energy sources, such as nuclear power, tides, hydro, and wind. Due to the abundance of solar energy throughout the world, its low cost, and environmental friendliness, it has piqued the interest of academia and industry [3]. Solar energy is harnessed through photovoltaic and solar thermal collectors. The latter is a promising solar energy harvesting technology that could be used for a variety of purposes, including domestic hot water, solar thermal generation, industrial cooling, seawater desalination [4], and electricity generation, among other things [5]. The solar selective absorber surface is the vital component of the solar thermal collector because it absorbs high radiant energy in the UV–Vis–NIR range of the solar spectrum and exhibits low emittance in the infrared range [6,7]. Photo-thermal conversion efficiency requires high temperature, and hence operating temperatures of the collectors can rise up to 1100 °C. However, as the temperature rises, the loss of thermal radiation energy increases, and the surface's structure and performance are affected to a large extent [8]. Zhiyan Yang et al. investigated the solar selectivity and air thermal stability of a spray-fabricated cobalt–nickel–iron oxide coating. The thermal stability of the two-layer $Ni_{0.9}Fe_{0.1}Co_2O_y$ coatings was evaluated by continuously heating at 500 °C in the air for 48 h. According to this report, the solar absorptance (α) remained unchanged at 0.93, while the emittance (ε) increased gradually from 0.11 to 0.30 [9]. Xiang-Hu et al. reported the structure, optical properties, and thermal stability of Al_2O_3-WC nanocomposite ceramic spectrally selective solar absorbers, which exhibit α of 0.94 and ε of 0.08 at 600 °C. Based on their report, the absorber exhibits good thermal stability in a vacuum at 600 °C for 5 h. The absorber seems to exhibit good thermal stability in a vacuum at 600 °C for 5 h [7]. The operating temperature of the most common solar absorbing coatings is between 200 and 600 °C. As a result, a type of solar coating with exceptional thermal stability is sorely needed in environments with high temperatures (T > 600 °C) [5].

The most commonly used methods in the world for preparing solar selective coatings include magnetron sputtering, paint coating, and sol-gel [10,11]. Yuping Ning et al. used DC magnetron sputtering to fabricate a NiCrAlO/Al_2O_3 solar selective coating, which exhibits high absorptance and low emittance of 0.964 and 0.066 at 25 °C [12]. Vasiliy Pelenovich et al. demonstrated the possibility of using non-equilibrium reactive RF magnetron sputtering to deposit graded solar selective absorbers. The authors record the highest absorptance and emittance at 0.909 and 0.0670, respectively [13]. To enhance the thermal stability of the solar selective metal/dielectric multilayer, Ying Wu et al. employed a multi-target magnetron sputtering method to form Cu, SiO_2, and Cr layers, whereas the Al_2O_3 layer was formed by atomic-layer-deposition (ALD). According to the authors, the as-deposited sample showed α of ~0.954 and ε of ~0.196 (773 K), demonstrating its good optical properties. After heat treatment at 500 °C for 72 h, α drops from ~0.033 to 0.951, while ε decreases from ~0.028 to 0.168 [14]. Adiba et al. investigated the structural and optical properties of sol-gel-synthesized NiO nanoparticles for selective solar absorbers and transparent heat mirror applications. The authors determined the optical band gap of the nanoparticles using UV-Vis absorption spectroscopy and discovered that their absorption edge is in the ultraviolet region of the solar spectrum, confirming their potential for use as selective solar absorbers and transparent heat mirrors [15]. Qihua et al. demonstrated that a (sol-gel prepared) reduced-graphene-oxide-based, spectrally selective absorber (rGO-SSA) has a low thermal emittance (ε = 0.04) and a high solar absorption of α = 0.92 at 800 °C [16]. The CoCuMnOx spinel ceramic film was deposited onto stainless steel 304 through the sol-gel dip coating method to form a solar selective coating that exhibits a selectivity of 0.85 [17]. Tesfamichael et al. synthesized and characterized a FeMnCuOx particle-based solar selective absorbing paint coating. Black carbon pigment was combined with silicone and phenoxy resin to form the coating [18].

Magnetron sputtering technology produces a coating with excellent bonding and optical properties, but it requires a vacuum environment, which in turns requires expensive equipment for mass production [19]. Solar absorbers prepared using paint and sol-gel methods suffer from a lack of adhesion between the film and the substrate, and they exhibit high emission, which has a significant negative effect on the absorber's performance [20,21].

Therefore, the hydrothermal method may be a better alternative because it has several advantages that overcome some of the above-mentioned challenges. These include low process cost, simplicity, pollution-free operation, and ease of application on a large scale [3]. As a result, the method was used to treat the surface of the stainless steel (SS) in this study in order to enhance its solar absorption property and to investigate the effect of annealing temperatures on the structural and optical properties of the treated surface. Indeed, due to its superior qualities compared to other metallic systems, SS is widely used in a wide variety of applications [22]. Stainless steel (SS) is often used in the fabrication of solar absorbers and can be rarely corroded under normal temperature and alkaline conditions. It has been reported that the corrosion process of the SS can be accelerated by hydrothermal conditions, leading to a special nano/microstructure oxide surface. The hydrothermal condition is very sensitive to film preparation parameters, such as time and temperature, which are very useful for obtaining the desired morphology and exploring an improved new optical phase of the material. For this reason, the hydrothermal heat treatment has been demonstrated to be a feasible technique to prepare solar selective absorbers for a photo-thermal conversion application [3].

Thermal stability of selective solar absorber coatings is critical, as the absorber degrades over time at operating temperatures when exposed to vacuum or air, reducing the life of the absorber and eventually resulting in failure [23–25]. Thermal stability testing in the presence of air is critical if the vacuum is breached [26]. Herein, we report the thermal stability of stainless steel (SS) solar absorbers that are hydrothermally treated and annealed in the temperature range between 300 and 700 °C.

2. Materials and Methods

2.1. Materials

Six sheets of stainless steel (434-L. SAE Grade) with square shapes of size 2.00 cm × 2.00 cm, NaOH in pellet form (500 g, Semiconductor Grade, 99.99% Trace metals basis) and solvents such as ethanol (200 Proof, Anhydrous, ≥99.5%) and acetone (Laboratory Reagent, ≥99.5%) were obtained from Sigma Aldrich. Teflon-line autoclaves (with 4 cm of diameter and 6 cm of height) used for hydrothermal treatment were obtained from KIMIX Chemical & Lab Supplies (Ruco bank unit 13, Boston circle airport Industrial north, Western Cape, 7525 South Africa). Chemical products such as ethanol, acetone, and NaOH in pellet form were of analytical grade and hence used without any further purification.

2.2. Methods

The hydrothermal technique was used to treat six sets of stainless steel (SS). The treatment process of the SS is detailed elsewhere [3]. Briefly, the SS was cleaned in ethanol, followed by acetone, and finally rinsed using deionized water. The sample in the autoclave in the alkaline solution was heated in a laboratory oven for 1 h at 200 °C to modify its surface layer, thus forming a film of different structure and composition.

To determine the thermal stability of the treated SS solar absorber, five specimens with the obtained films were isothermally heated between 300 °C and 700 °C in air in a furnace (Elite Thermal Systems Limited model TSH12/50/610-2416CG) for 2 h at each selected temperature: 300, 400, 500, 600 and 700 °C. The temperature was raised from room temperature to the required temperature at a rate of 9 °C/min and then cooled at a rate of 10 °C/min after attaining the required duration. The used furnace has a proportional–integral–derivative (PID) temperature control system to improve the accuracy of the annealing process; we estimated an average of 0.1 °C in precision after performing a number of experiments using the same furnace. One film was not annealed in order to serve as the reference of the sample.

2.3. Structural and Optical Characterization

The structural composition of samples was investigated by using X-ray diffraction (Bruker AXS D8 X-ray diffractometer, Cu-Kα radiation of average wavelength ~1.54 Å, operating at 40 kV and 35 mA in Bragg-Brentano geometry, Billerica, MA, USA). XRD measurements provide significant information on the width and grain size of crystallites, and phase's identification [27]. The morphology and elemental composition of all samples were studied by High Resolution–Scanning Electron Microscopy (HR-SEM: Hitachi X-650 electron microscopy unit with a resolution limit of 0.12 nm, coupled with the Energy Dispersive X-rays Spectroscopy (EDS), Chiyoda City, Japan). The optical reflectance of the samples was evaluated in the wavelength range of 0.25–2.50 µm by Cary series 5000 UV-Vis-NIR double beam spectrophotometer, while the reflectance in the thermal wavelength zone of 3.00–20.00 µm was characterized by Thermo-Nicolet 8700 Fourier transform infrared (FT-IR) spectroscopy.

Solar absorptance (α) values for the samples were calculated using [8],

$$\alpha = \frac{\int_{0.2}^{2.5}[1 - R(\lambda)]I_{sol}(\lambda)d\lambda}{\int_{0.2}^{2.5} I_{sol}(\lambda)d\lambda} \tag{1}$$

where R, λ, and I_{sol} denote reflectance, wavelength, and direct normal solar irradiance, respectively, as defined by ISO standard 9845-1 (1992), with an air mass (AM) of 1.5. For opaque materials, the absorptance (α) is expressed in terms of the total reflectance (R_λ).

$$\alpha = 1 - R_\lambda \tag{2}$$

The thermal emittance (ε) was obtained using [28],

$$\varepsilon = \frac{\int_{3.0}^{20}[1 - R(\lambda, T)]B(\lambda, T)d\lambda}{\int_{3.0}^{20} B(\lambda, T)d\lambda} \tag{3}$$

where B (λ, T) denote radiance of a blackbody at temperature T.

3. Results and Discussion

3.1. X-ray Diffraction (XRD)

The X-ray diffraction profile of the as-obtained (Figure 1a) and annealed films (Figure 1b–f) have been indexed to the Fe_2O_3 phases (JCPDS card no. 00-039-1346) and (JCPDS card no. 00-033-0664). Figure 1 shows two different sets of peaks with different structures of the (a) as-obtained and (b–f) annealed film within the temperature range of 300–700 °C. The crystal structures of the (a) as-obtained and (b–f) film annealed at different temperatures were evaluated within the 2θ angular range of 15–90° by X-ray Diffraction. The XRD analysis for the as-obtained and annealed films were tabulated in Tables A1–A6, respectively (See Appendix A).

The results of the analysis, such as inter-planar distance (d), crystallites grain size (ϕ), full width at half maximum (FWHM), lattice constant (a) and other XRD values for the samples, were evaluated and are summarized in Table 1.

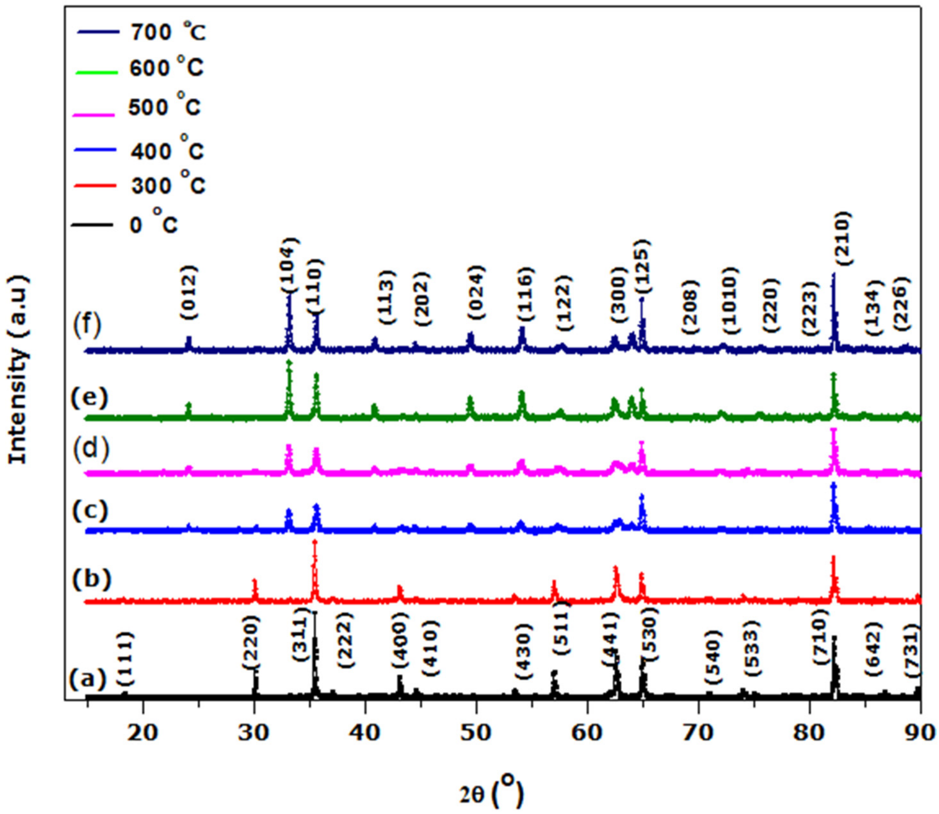

Figure 1. XRD patterns of the (**a**) as-obtained (0 °C) and films annealed for 2 h in air at: (**b**) 300 °C, (**c**) 400 °C, (**d**) 500 °C, (**e**) 600 °C and (**f**) 700 °C. The figure revealed the formation of the new peaks and changes (width and height of the peaks) that occurred on them as the annealing temperature increases.

Table 1. XRD results summarized for the (a) as-obtained (0 °C) and films annealed for 2 h in air at: (b) 300 °C, (c) 400 °C, (d) 500 °C, (e) 600 °C and (f) 700 °C.

Sample	t (°)	Dd/d_{bulk}	FW (Rad)	ϕ (nm)	ε (10^{-1})	σ (GPa)	δ (nm^{-2})	a (Å)
a	0	0.020	0.024	67	1.2	−2.9	2.2×10^{-4}	8.45
b	300	0.007	0.025	66	4.4	−103.2	2.3×10^{-4}	7.27
c	400	−0.006	0.027	60	5.1	−119.2	2.8×10^{-4}	7.61
d	500	0.002	0.032	51	4.6	−107.8	3.9×10^{-4}	7.64
e	600	0.002	0.038	43	5.2	−121.6	5.3×10^{-4}	7.66
f	700	0.002	0.043	38	5.2	−120.6	6.9×10^{-4}	7.64

The inter-planer distances (*d*) were calculated for spectra using Bragg's law [29],

$$d = \frac{n\lambda}{2sin\theta} \tag{4}$$

where λ~1.541 Å is the wavelength of Cu-K radiation, n = 1 and θ is the Bragg angle (half of the measured diffraction angle). As shown in Table A1 (See Appendix A) the average ratio of Dd/d_{bulk} (where $Dd = d exp - d_{bulk}$) is constantly positive, ranging from 0.002 to 0.007 for all *hkl* reticular plans, except for the film annealed at 400 °C, which shows a negative value (−0.006). This indicated that the peaks of the film annealed at 400 °C are subjected to small compressive strain at the various crystallographic directions, whereas the peaks of the film prepared and annealed at 300, 500, 600 and 700 °C are under tensile strain conditions. The average grain size of the crystallite (Ø) was evaluated using Debye–Scherrer, expressed as [30],

$$\langle Ø \rangle = \frac{0.9\,\lambda}{D\theta_{\frac{1}{2}}\cos\theta_B} \tag{5}$$

where λ, $D\theta_{1/2}$ and θ_B are the X-ray wavelength (~1.541 Å), Full Width at Half Maximum (FWHM) in radian, and Bragg's diffraction angle, respectively. The FWHM of the treated (as-obtained) film is 0.024 (rad), whereas the film annealed at different temperatures records FWHM in the range of 0.025–0.043 (rad). The average grain size of the crystallite (Ø) for the as-obtained film is 67 nm, whereas the annealed film at various temperatures records Ø in the range of 66–38 nm, as shown in Table 2. Similarly, it is observed (Table 2) that as the annealing temperature increases, the average grain sizes decreases, whereas the FWHM tends to increase. The increment in FWHM can be attributed to island coalescence [31], whereas the reduction in Ø can be attributed to reduction in surface roughness of the film [3]. Coalescence is a process whereby small crystallites combine to form larger crystalline particles. The process causes major grain growth, which influences porosity and reduction in surface roughness [32].

Table 2. Variation of the film pore's diameter with increment in annealing temperature.

Sample	Annealed Temp (°C)	Pore Diameter (µm)
a	0	0.47 ± 0.06
b	300	0.53 ± 0.07
c	400	0.49 ± 0.11
d	500	0.52 ± 0.10
e	600	0.59 ± 0.11
f	700	0.69 ± 0.11

The dislocation density (δ) was obtained from (Ø) using [33–36].

$$\delta = \frac{1}{()^2} \tag{6}$$

where Ø is the average grain size of the crystallite. The δ was found to be 2.2×10^{-4} nm^{-2} for the as-treated film, while 2.3×10^{-4}, 2.7×10^{-4}, 3.9×10^{-4}, 5.4×10^{-4}, and 6.9×10^{-4} nm^{-2} were obtained for the films annealed at 300, 400, 500, and 700 °C, respectively. It is observed that the film annealed at 700 °C exhibited a smaller value of δ (6.9×10^{-4} nm^{-2}), which implies that the film had fewer lattice defects and good crystalline qualities [37].

The lattice constants (a) were calculated using [3],

$$a = d_{hkl}^{exp} \times \sqrt{h^2 + k^2 + l^2} \tag{7}$$

where d_{hkl}^{exp} is the experimental inter-planar spacing obtained from Bragg's law, and h, k, and l are the Miller indices denoting the plane. The bulk lattice constant (result obtained from database) of the as-obtained film is ~8.35 Å (Fe_2O_3, JCPDS card no. 00-039-1346), whereas the corresponding experimental average lattice constant for this film (annealed film) was estimated to be ~8.45 Å, which is a little bit higher than the bulk value. The obtained bulk lattice constant of the film annealed is ~5.04 Å (Fe_2O_3, JCPDS card no. 00-033-0664), whereas the corresponding experimental lattice constant of this film annealed at various temperatures (Appendix A Table A1) was estimated to be in the range of ~7.27 to 7.66 Å. The small differences between the experimental lattice constant (a_{exp}) and the corresponding bulk lattice constant (a_{bulk}) may be due to the effects of tensile strains between the substrate and film (Fe_2O_3).

The strains (ε) and stress (σ) are given as,

$$\varepsilon = \frac{a_{exp} - a_{bulk}}{a_{bulk}} \tag{8}$$

$$\sigma = -2.33 \times 10^{11} \left[\frac{a_{exp} - a_{bulk}}{a_{bulk}} \right] \tag{9}$$

where a_{exp} and a_{bulk} are the calculated experimental and bulk lattice constant of the as-obtained and annealed films.

The strains (ε) and stress (σ) along the *a-axis* in the as-treated film were found to be 1.2×10^{-1} and −2.9 GPa, whereas the annealed film at 300, 400, 500, 600, 700 °C records the values of the strain (ε) and stress (σ) at 4.4×10^{-1}, 5.1×10^{-1}, 4.6×10^{-1}, 5.2×10^{-1}, 5.2×10^{-1} and −103.2, −119.2, −107.8, −121.6, and −120.6 GPa, respectively, using Equations (8) and (9). The stress (σ) negative sign obtained for the films annealed shows that the film is in a state of compressive stress [29]. The presence of the compressive stress can be attributed to the lattice mismatch between the bulk materials (~5.04 Å) and films annealed (in the range of~7.27 to 7.66 Å). According to the reports, the lattice mismatch between the film and the substrate results in a variety of strains of varying degrees [38].

However, examining the ε and σ in the film provides significant information on the evolution of the defect, which is critical for better understanding and optimizing the electrical and optical properties of the film. It has been reported that the band structure of a material can change with the strain field, thereby changing its optical properties [39]. Therefore, the purpose of observing both ε and σ in this study is to determine the level of cracks and other defects in the film treated (as-obtained film) and annealed in the range of 300–700 °C. Fortunately, the obtained results of ε and σ in the films are not significant enough to affect the optical performance of the films (absorber surface).

3.2. Scanning Electron Microscopy (SEM) Analysis

Figure 2 reports the surface morphology images of the (a) as-obtained and (b–f) films annealed at 300, 400, 500, 600 and 700 °C, respectively. SEM images confirm the presence of micropores distributed across the surfaces of all films. It has been reported that micropores on the surface of a material minimize surface reflection, which in turn influences photoabsorption by trapping the incident light and subjecting it to multiple reflections [3].

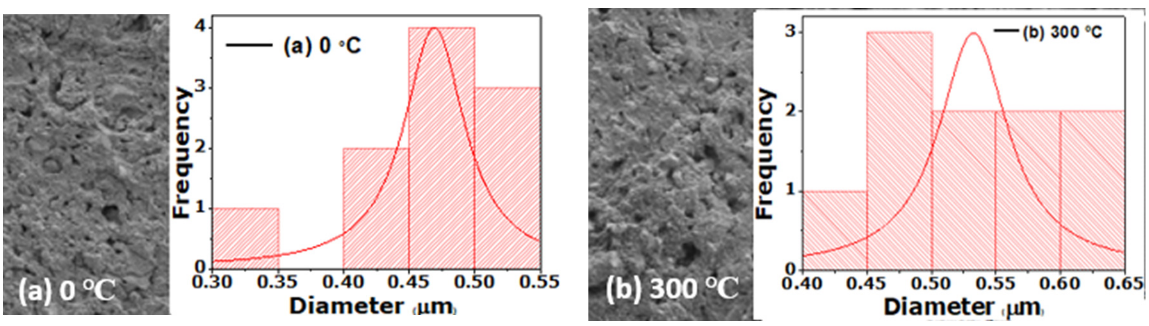

Figure 2. *Cont.*

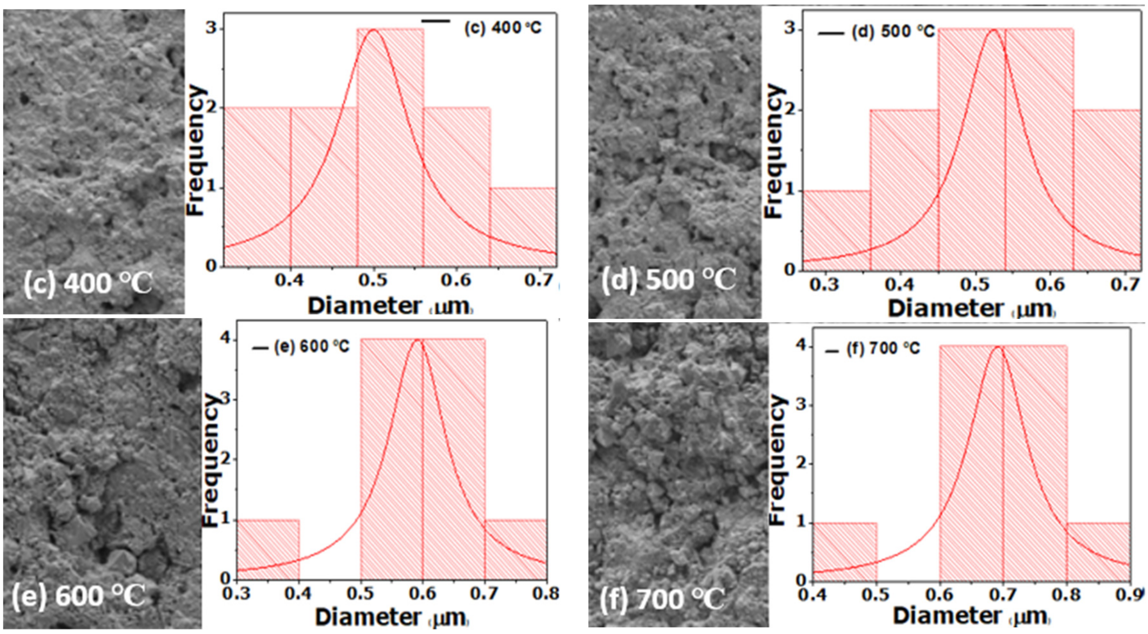

Figure 2. HR-SEM images of the (**a**) as-obtained (0 °C) and films annealed for 2 h in air at: (**b**) 300 °C, (**c**) 400 °C, (**d**) 500 °C, (**e**) 600 °C and (**f**) 700 °C. The insert figures revealed the size of the pores on the film surfaces.

After the digitization of various HR-SEM images, the diameter of the average size of the pores was found to be 0.47 ± 0.06 µm for the as-treated film, while 0.53 ± 0.07, 0.49 ± 0.11, 0.52 ± 0.10, 0.59 ± 0.11, and 0.69 ± 0.11 µm were obtained for the annealed films at 300, 400, 500, and 700 °C, respectively. Table 2 shows that as the annealing temperature increases, the size of the pores on the film increases. However, films annealed at 400 and 500 °C (sample c & d) are not in trend, and this could be the effect of different Teflon-line autoclaves used for film treatment via the hydrothermal technique.

3.3. Energy-Dispersive X-ray Spectroscopy (EDS) Analysis

The elemental composition of the (a) as-obtained and (b–f) films annealed at 300, 400, 500, 600, and 700 °C were determined using EDS. All samples contain similar elemental components (i.e., C, Cr, Fe, and O) but have varying atomic percentages. The variation in the atomic percentage (%) for each sample is summarized in Table 3, while Figure 3 illustrates the EDS analysis.

Table 3. EDS elemental analysis of the (a) as-obtained (0 °C) and films annealed for 2 h in air at: (b) 300 °C, (c) 400 °C, (d) 500 °C, (e) 600 °C and (f) 700 °C.

Elements	Atomic Percentage (%)					
	a	b	c	d	e	f
C	10.24	13.73	9.57	10.00	10.20	19.71
Cr	9.22	8.67	9.53	6.54	4.87	5.40
Fe	25.94	24.25	27.48	31.41	32.87	26.22
O	54.60	53.35	53.42	52.05	52.05	48.67
Total	100	100	100	100	100	100

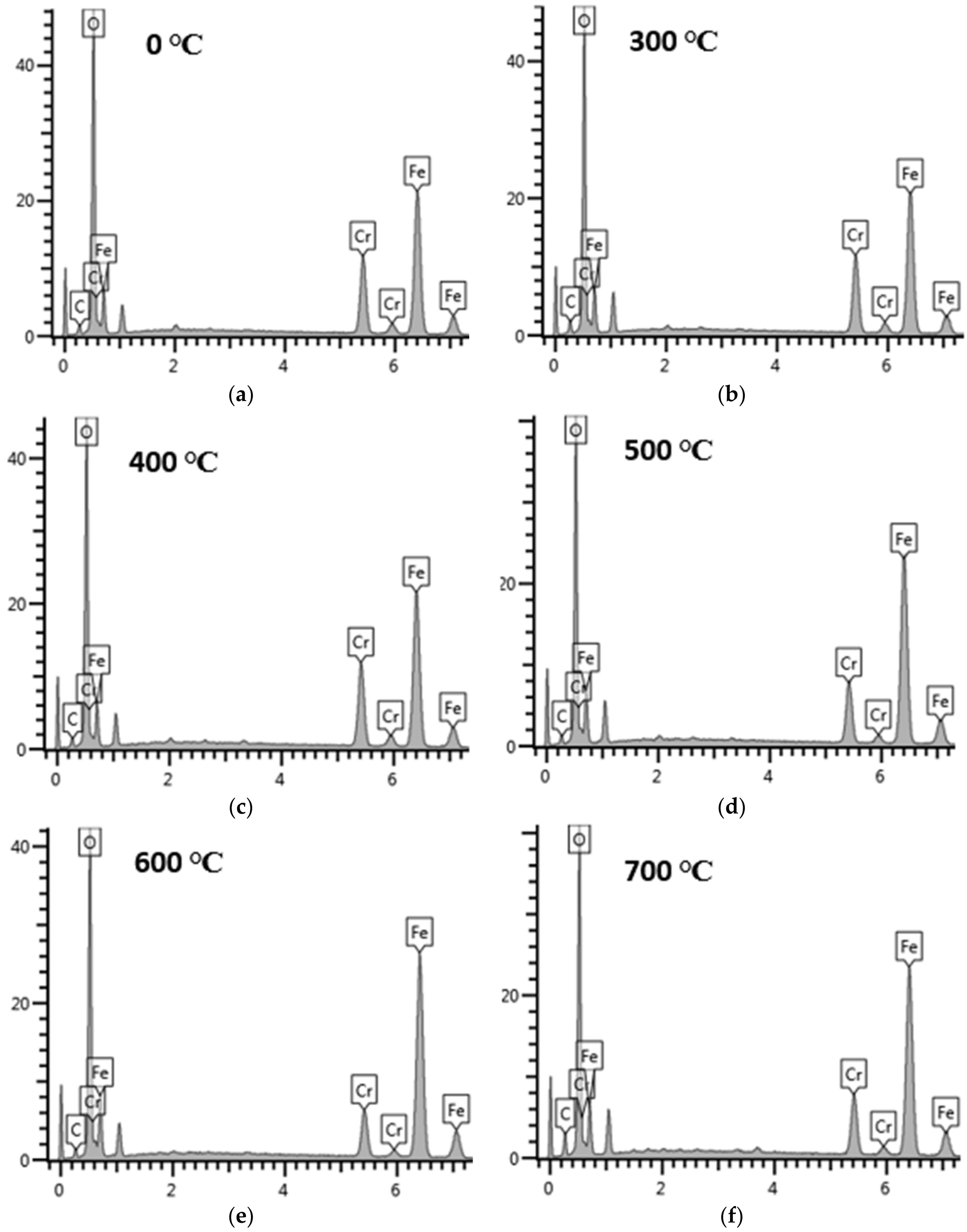

Figure 3. EDS patterns of the (**a**) as-obtained (0 °C) and films annealed for 2 h in air at: (**b**) 300 °C, (**c**) 400 °C, (**d**) 500 °C, (**e**) 600 °C and (**f**) 700 °C. The figure depicts the variation in elemental composition of the films as the annealing temperature varied.

It is observed that both as-obtained and annealed films contain Carbon (C), Chromium (Cr), Iron (Fe) and Oxygen (O), but the atomic percentage (%) of these elements in the films varies. It can be observed from Table 4 that the as-obtained film (a) contains the highest atomic % of O (54.60%), whereas the film annealed at 700 °C (f) exhibits the lowest atomic % of O (48.67%). This confirms that as the annealing temperature increases, the atomic % of O decreases. Table 3 revealed that the film annealed at 600 °C (e) contains the highest atomic % of Fe (32.41%), whereas the film annealed at 300 °C (b) has the lowest atomic % of Fe (24.25%). It is also observed that the atomic % of Cr in the film decreases from 9.22 to 8.67% when the film is annealed from 200 to 300 °C and later increases to 9.53% at 400 °C.

Table 4. Absorptance (α) and emittance (ε) of the (a) as-obtained and (b–f) film annealed for 2 h in air at different temperature.

Sample	T (°C)	α	ε	α/ε (η)
a	0	0.938	0.431	2.176
b	300	0.941	0.403	2.335
c	400	0.922	0.333	2.769
d	500	0.917	0.274	3.347
e	600	0.892	0.179	4.983
f	700	0.884	0.179	4.939

However, among the elemental components of the films, Cr and Fe, which are transitional metals, play a vital role in minimizing the thermal radiation from the material. Indeed, the presence of transitional metal in a material helps to enhance its optical infrared reflectance property, which is required to achieve high selectivity for photo-thermal conversion applications. However, the element O also plays a significant role in the absorption property of a metal. Metal atoms are composed of a metallic ion's d-shell, which is partially filled. When this metallic ion reacts with oxygen, the electrons become localized, forming metallic oxide, a new material with a high absorption capacity. Transition metals' high infrared reflectance is due to the free electrons contained within their atoms, whereas their absorption is influenced by the bonded electrons. Thus, the oxidized surface of the metal exhibits a high absorption characteristic, whereas the transitional base metal exhibits a high infrared property, which aids in minimizing thermal emission loss from the absorber surface; thus, the combination of the two phases results in a good selective absorber with the required optical properties for photo-thermal conversion applications [3].

3.4. UV-Vis-NIR Diffuse Reflectance Analysis

The optical reflectance of the (a) as-obtained and (b–f) films annealed for 2 h in air at different temperatures was investigated by analyzing UV-Vis-NIR diffuse reflectance data in the wavelength region of 0.25–2.50 µm, as illustrated in Figure 4. It is observed that the film annealed at 300 °C (Figure 4b) exhibits the lowest reflectance of ~7%, whereas the film annealed at 700 °C exhibits the highest reflectance of about 20%. Figure 4 further shows that as the annealing temperature increases, the reflectance of the films also increases, which confirms the negative effect of the high annealing temperature on the reflectivity behavior of the film. It has been reported that the lower a surface's reflectivity is in the short wavelengths of the solar spectrum, the greater its absorptance value, whereas the opposite is true in the longer wavelengths of the thermal spectrum; i.e., the higher the reflectivity of a surface in the mid/long IR wavelength region, the lower the emissivity of a material. Indeed, the two major requirements for achieving high selectivity of a material for photo-thermal conversion application are the low reflectivity of the incident solar radiation and the high reflectivity of the thermal radiation [3].

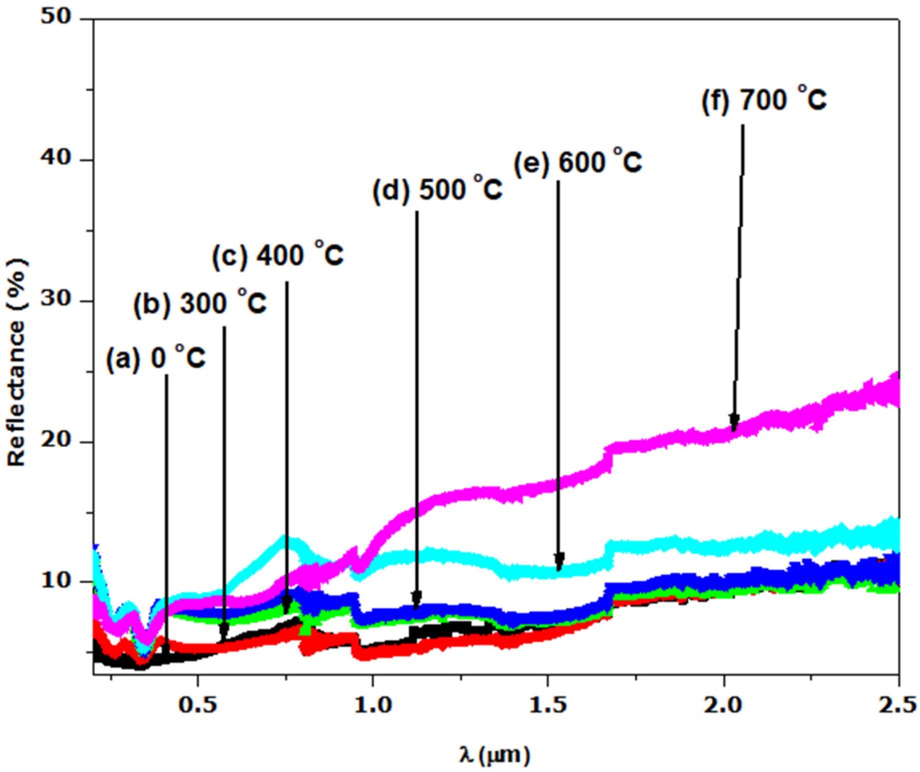

Figure 4. UV-vis-NIR reflectance spectra of the (**a**) as-obtained (0 °C) and annealed films for 2 h in air at: (**b**) 300 °C, (**c**) 400 °C, (**d**) 500 °C, (**e**) 600 °C, and (**f**) 700 °C. The variation of reflectance with annealing temperature at UV-Vis region depicted in the figure implies an improvement in absorptance as the temperature increases.

The decrease in the reflectance spectra (%R) of the films in the UV-Vis-NIR wavelength zone can be attributed to surface oxidation induced by the NaOH used in the hydrothermal treatment, as confirmed by EDS analysis. Another possible explanation for the decrease in reflectance in this wavelength zone is the presence of micropores on the surface of the films, as revealed by SEM analysis [3].

3.5. FT-IR Diffuse Reflectance Analysis

The optical reflectance of the (a) as-obtained and (b–f) films annealed for 2 h in air at different temperatures was studied by analyzing the FT-IR diffuse reflectance data in the wavelength zone of 3.0–20.0 μm, as shown in Figure 5. It is observed that the film annealed at 700 °C (Figure 5f) exhibits the highest reflectance of ~90%, whereas the as-obtained film exhibits the lowest reflectance of about 60%. Figure 5 further shows that as the annealing temperature increases, the reflectance of the film also increases. The reflectivity reduction at IR wavelength zone causes high emissivity to the absorber material, which in turn reduces its selectivity. Hence, decrement in reflectivity in the IR region does not favor solar selective absorber material for photo-thermal conversion application.

The decrease in reflectance spectra (%R) at the IR wavelength zone of the film can be attributed to the increment in atomic % of oxygen (O), as revealed by EDS results. The atomic % of the oxygen of the film annealed at 700 °C is 48.67%, and the value keeps increasing up to 54.60% (film annealed at 0 °C) as the annealing temperatures decrease, as revealed in Table 3. Indeed, increased oxidation has been shown to result in a decrease in reflectivity in the mid/far-infrared wavelength region, causing high emissivity on a material [3].

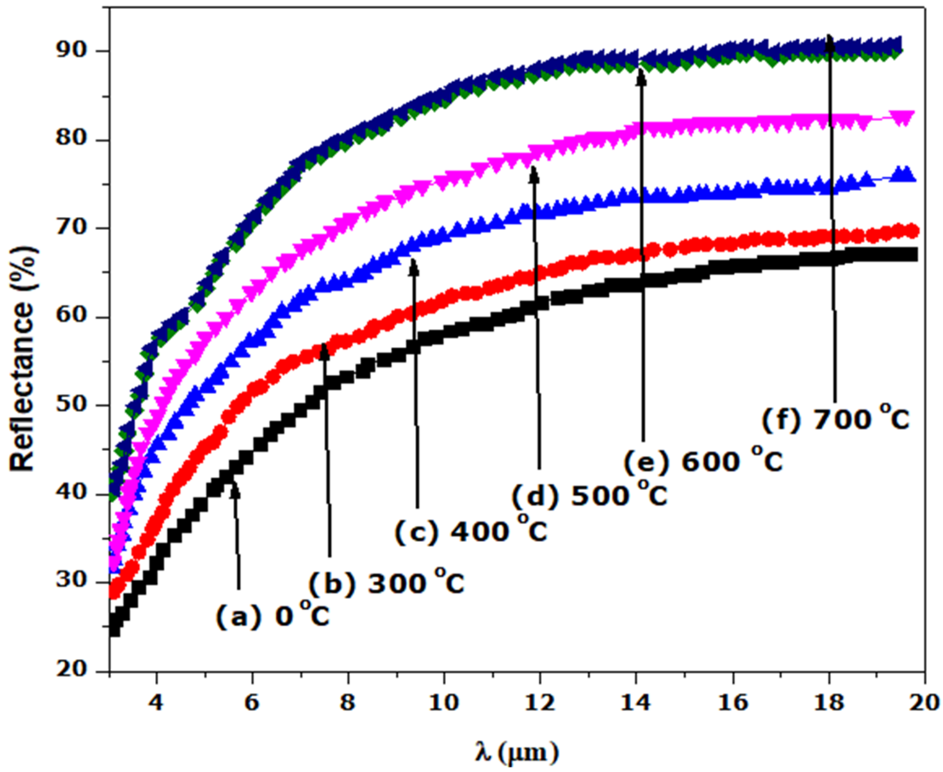

Figure 5. FT-IR reflectance spectra of the (**a**) as-obtained (0 °C) and annealed films for 2 h in air at: (**b**) 300 °C, (**c**) 400 °C, (**d**) 500 °C, (**e**) 600 °C, and (**f**) 700 °C. The variation of reflectance with annealing temperature at IR region is revealed in this figure.

3.6. Absorptance (α) and Emittance (ε) Evaluation

Solar absorptance (α) was calculated for the films using Equation (1) and weighted by solar irradiance based on the standard air mass 1.5 solar spectrum in the wavelength range 0.25–2.50 µm, while thermal emittance (ε) was calculated using Equation (3) and measured Blackbody reflectance data [3]. The "α" and "ε" results of the films are shown in Table 4, which reveals that as the annealing temperature increases, the absorptance increases first from 0.938 (as-obtained SS) to 0.941 (annealed) at 300 °C and then continuously decreases as the temperature proceeds to 700 °C, where the film exhibits the lowest absorptance of 0.884. It is similarly observed that as the annealing temperature increases, the film emittance decreases in the range from 0.431 to 0.179, as shown in Table 4. The decrease in film absorptance is attributed to its low surface reflectivity in the UV-Vis-NIR spectrum, whereas the decrease in emittance is attributed to high surface reflectivity in the mid/far-IR wavelength zone, as illustrated in Figures 4 and 5. The error/standard deviation on these data is ±0.11.

The increase in "α" is beneficial to the solar absorber's properties, whereas the increase in "ε" is detrimental to the solar absorber's surface. This is because a high emittance value results in a greater loss of energy absorbed by the surface [3].

However, Figure 6 has been plotted to show the variation of α, ε, and η of the films with an increment in annealing temperatures. Figure 6 reveals that both the absorptance (α) and emittance (ε) of the films tend to decrease as the annealing temperature increases, whereas the selectivity factor (η) enclosed in Figure 6 tends to increase. The selectivity factors (η) of the films were evaluated and found to vary from 2.176 to 4.983 ± 1.26, as illustrated in Figure 6. This increment in η implies an improvement in the selectivity of the film annealed at 700 °C.

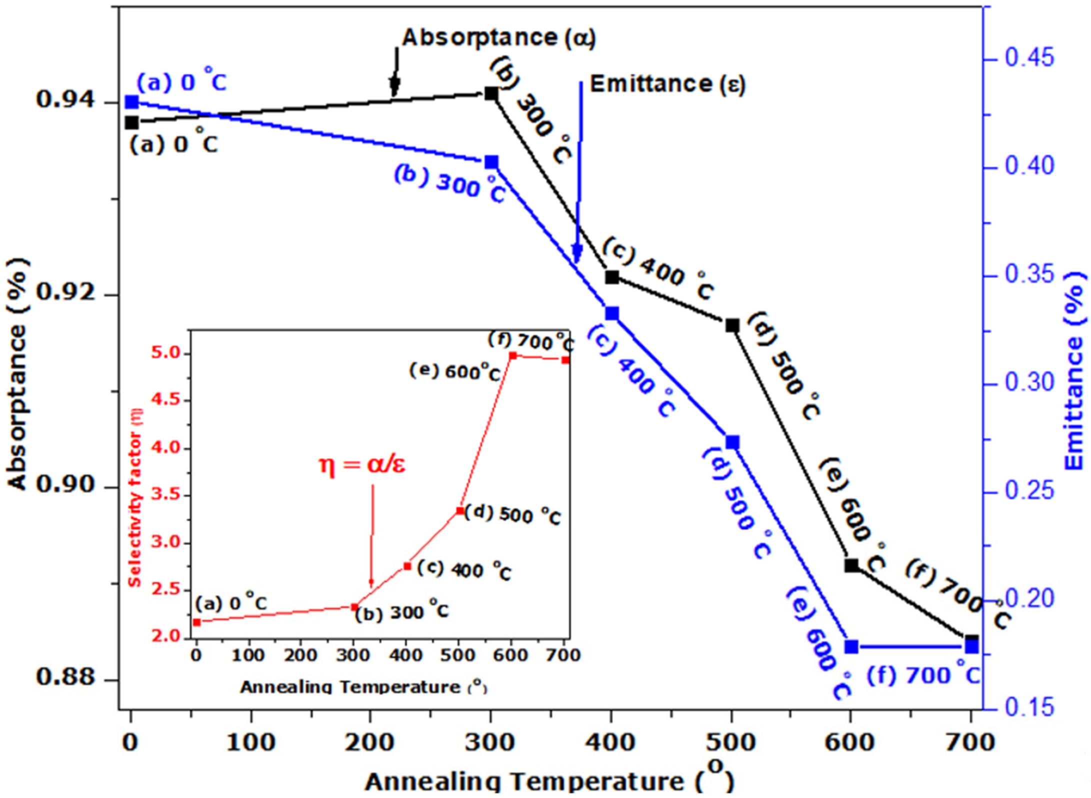

Figure 6. Variation of absorptance (α), emittance (ε) and selectivity factor (η) of the (**a**) as-obtained (0 °C) and annealed films at: (**b**) 300 °C, (**c**) 400 °C, (**d**) 500 °C, (**e**) 600 °C, and (**f**) 700 °C. The insert figure depicts the improvement in the selectivity (α/ε) of the annealed films.

4. Conclusions

We have treated the surface of stainless steel to enhance its solar absorption property using a hydrothermal technique. Following the thermal treatment at different annealing temperatures, the SS absorber was characterized. The SEM images reveal micropores with decreasing grain sizes and increasing full width at half maximum (FWHM) when annealing temperature is increased, as confirmed by XRD analysis. The EDS spectrum indicates the presence of the transitional elements Cr and Fe, which were evident in the optical response. The SS absorber exhibited a lower reflectance at the UV-VIS-NIR wavelength zone, and this can be attributed to the presence of micropores, which were evident in the SEM images. The optical reflectance of the annealed films at the far-IR wavelength zone were high (60 to 90%), resulting in the obtained minimum thermal emission of the annealed SS absorbers. The major components of the as-treated and annealed film that play a significant role in enhancing the selectivity of the SS absorber are Cr, Fe, and O, as evidenced by the EDS result. Cr and Fe are transitional metals that help to enhance the optical infrared reflectance property of a metal/film, whereas element O (deposited on SS absorber through NaOH used during the hydrothermal treatment) enhances the absorption property of the SS absorber. Thus, the oxidized surface (Fe_2O_3) of the SS exhibits a high absorption characteristic, whereas Fe and Cr exhibit a high infrared reflectance property, which aids in minimizing thermal emission loss from the absorber surface; thus, the existence of these elements (Fe and Cr) in film results in a good selective absorber with the required optical properties for photo-thermal conversion applications.

The as-obtained SS absorbers exhibit spectra selectivity of 2.176 (0.938/0.431), whereas SS annealed at 700 °C exhibits 4.939 (0.884/0.179). These results indicate a significant improvement in the selectivity (absorptivity/emissivity) of the SS annealed at 700 °C. Hence, the annealed SS absorber could be a promising candidate for a photo-thermal conversion application.

Author Contributions: S.A.A.: Investigation, Data curation, Formal analysis, Writing—original draft, Writing—review & editing. R.A.: Data curation, Writing—review & editing. J.S.: Writing—review & editing. S.K.: Writing—review & editing. S.H.: Writing—review & editing. Z.Y.N.: Writing—review & editing. M.M.: Resources, Supervision, Project administration, Funding acquisition. All authors have read and agreed to the published version of the manuscript.

Funding: This research received no external funding.

Institutional Review Board Statement: Not applicable.

Informed Consent Statement: Not applicable.

Data Availability Statement: Not applicable.

Acknowledgments: This work was supported by the UNESCO-UNISA Africa Chair in Nanosciences & Nanotechnology, and the National Research Foundation (NRF) of South Africa. We gratefully acknowledge the help provided by the Department of Materials Division (MRD), iThemba-LABS, South Africa, for the provision of the research lab and equipment. This research did not receive any specific grant from funding agencies in the public, commercial, or not-for-profit sectors.

Conflicts of Interest: The authors declare that they have no known competing financial interests or personal relationships that could have appeared to influence the work reported in this paper.

Appendix A

Table A1. XRD values and crystallites size of the as-obtained film (Figure 1a).

Hkl	θ_{bulk} (°)	θ_{exp} (°)	d_{bulk} (Å)	d_{exp} (Å)	Dd/d_{bulk}	FWHM (rad)	Ø (nm)	a (Å)
111	9.192	9.045	4.822	4.906	0.018	0.022	64.077	8.498
220	15.121	15.062	2.593	2.974	0.147	0.023	63.925	8.411
311	17.816	17.724	2.518	2.534	0.006	0.023	63.595	8.405
222	18.625	17.745	2.412	2.526	0.047	0.023	63.437	8.749
400	21.643	21.555	2.089	2.099	0.005	0.023	65.083	8.396
410	22.353	22.315	2.026	2.032	0.003	0.024	62.874	8.379
430	27.463	26.733	1.670	1.716	0.027	0.024	63.928	8.578
511	28.637	28.504	1.607	1.615	0.005	0.026	61.419	8.391
441	31.998	31.301	1.454	1.484	0.021	0.025	65.069	8.527
530	32.537	32.484	1.432	1.434	0.002	0.023	70.286	8.364
540	36.202	35.492	1.304	1.326	0.017	0.024	70.717	8.489
533	37.237	37.036	1.273	1.279	0.005	0.026	66.656	8.583
710	40.711	41.124	1.181	1.171	−0.009	0.028	66.206	8.278
642	43.654	43.395	1.116	1.121	0.005	0.027	70.052	8.390
731	45.115	45.013	1.087	1.089	0.002	0.023	83.796	8.369

Table A2. XRD values and crystallites size of the annealed film at 300 °C (Figure 1b).

Hkl	θ_{bulk} (°)	θ_{exp} (°)	d_{bulk} (Å)	d_{exp} (Å)	Dd/d_{bulk}	FWHM (rad)	Ø (nm)	a (Å)
104	16.579	16.631	2.700	2.692	−0.003	0.024	61.648	11.097
110	17.806	17.759	2.519	2.526	0.003	0.024	60.604	3.572
202	21.759	21.644	2.078	2.105	0.013	0.025	60.934	5.954
116	27.046	26.941	1.694	1.700	0.004	0.025	63.404	10.479
122	28.715	28.651	1.603	1.607	0.002	0.025	64.543	4.819
300	31.996	31.395	1.454	1.479	0.017	0.025	63.921	4.436
125	33.014	32.429	1.414	1.436	0.016	0.026	63.522	7.867
1010	35.969	35.743	1.312	1.319	0.006	0.027	62.677	13.253
220	37.715	37.167	1.259	1.275	0.013	0.027	65.673	3.607
128	40.356	40.945	1.189	1.176	−0.012	0.025	73.594	9.764
226	44.271	43.129	1.104	1.127	0.021	0.026	74.046	7.473
042	45.673	45.114	1.077	1.087	0.009	0.028	71.089	4.862

Table A3. XRD values and crystallites size of the annealed film at 400 °C (Figure 1c).

Hkl	θ bulk (°)	θ exp (°)	d_{bulk} (Å)	d_{exp} (Å)	Dd/d_{bulk}	FWHM (rad)	Ø (nm)	a (Å)
012	12.068	12.079	3.684	3.680	−0.001	0.025	56.225	8.229
104	16.579	16.591	2.770	2.698	−0.026	0.026	56.139	11.124
110	17.806	17.829	2.519	2.516	−0.001	0.026	55.607	3.558
113	20.428	20.442	2.207	2.206	−0.001	0.026	56.317	7.316
202	21.759	21.855	2.078	2.069	−0.004	0.026	56.969	5.852
024	24.740	24.760	1.841	1.839	−0.001	0.027	56.223	8.226
116	27.041	27.037	1.694	1.695	0.0002	0.028	56.392	10.445
122	28.715	28.709	1.603	1.603	9.6×10^5	0.029	54.513	4.810
214	31.996	31.518	1.486	1.473	−0.008	0.028	57.595	6.752
300	33.014	32.478	1.454	1.435	−0.013	0.027	61.581	4.304
1010	35.969	36.059	1.312	1.309	−0.002	0.027	62.589	13.152
128	40.356	41.118	1.189	1.171	−0.015	0.029	62.641	9.730
134	42.458	42.624	1.141	1.138	−0.003	0.029	65.438	5.799
226	44.271	44.663	1.104	1.096	−0.007	0.025	78.051	7.269

Table A4. XRD values and crystallites size of the annealed film at 500 °C (Figure 1d).

Hkl	θ bulk (°)	θ exp (°)	d_{bulk} (Å)	d_{exp} (Å)	Dd/d_{bulk}	FWHM (rad)	Ø (nm)	a (Å)
012	12.068	12.080	3.684	3.680	−0.001	0.031	46.557	8.229
104	16.579	16.578	2.700	2.699	-1.4×10^5	0.031	46.658	11.132
110	17.806	17.679	2.519	2.536	0.007	0.031	46.299	3.587
113	20.428	20.362	2.207	2.214	0.003	0.032	47.054	7.343
202	21.759	21.733	2.078	2.080	0.001	0.032	47.445	5.884
024	24.690	24.758	1.841	1.839	−0.001	0.032	47.134	8.228
116	27.046	27.057	1.694	1.693	−0.001	0.033	47.406	10.438
122	28.665	28.734	1.603	1.603	−0.001	0.034	46.185	4.807
300	31.996	31.372	1.454	1.479	0.018	0.034	48.511	4.439
125	33.014	32.396	1.414	1.438	0.017	0.032	51.432	7.874
208	34.801	34.845	1.349	1.349	−0.001	0.033	51.759	11.121
1010	35.969	36.085	1.312	1.308	−0.003	0.035	49.561	13.143
220	37.715	37.875	1.259	1.255	−0.004	0.034	51.616	3.549
223	39.380	40.258	1.214	1.192	−0.018	0.030	60.142	4.914
210	41.469	41.177	1.163	1.169	0.006	0.031	58.655	11.931
134	42.458	42.479	1.141	1.141	−0.0004	0.035	54.494	5.816
226	44.271	43.795	1.104	1.113	0.009	0.033	58.229	7.384

Table A5. XRD values and crystallites size of the annealed film at 600 °C (Figure 1e).

Hkl	θ bulk (°)	θ exp (°)	d_{bulk} (Å)	d_{exp} (Å)	Dd/d_{bulk}	FWHM (rad)	Ø (nm)	a (Å)
12	12.068	12.077	3.684	3.682	−0.001	0.036	39.734	8.234
104	16.579	16.593	2.700	2.697	−0.001	0.036	39.917	11.121
110	17.806	17.818	2.519	2.518	−0.0003	0.037	39.720	3.561
113	20.428	20.444	2.207	2.205	−0.001	0.037	40.267	7.314
202	21.759	20.444	2.078	2.205	0.061	0.037	40.323	6.237
024	24.690	24.752	1.841	1.839	−0.001	0.038	40.575	8.228
116	27.046	27.064	1.694	1.693	−0.001	0.038	40.890	10.438
122	28.665	28.793	1.603	1.599	−0.003	0.039	40.081	4.797
300	31.996	31.265	1.454	1.485	0.021	0.039	41.900	4.454
125	33.014	32.474	1.414	1.435	0.015	0.037	44.226	7.858
208	34.801	34.598	1.349	1.357	0.005	0.038	44.468	11.187
1010	35.969	36.052	1.312	1.309	−0.002	0.039	43.028	13.155
220	37.715	37.758	1.259	1.258	−0.001	0.039	44.659	3.558
223	39.380	38.909	1.214	1.226	0.010	0.036	50.269	5.057
210	41.469	41.089	1.163	1.172	0.008	0.037	50.206	11.953
134	42.458	42.496	1.141	1.140	−0.001	0.039	47.325	5.815
226	44.271	44.345	1.104	1.102	−0.001	0.038	50.723	7.311

Table A6. XRD values and crystallites size of the annealed film at 700 °C (Figure 1f).

Hkl	θ bulk (°)	θ exp (°)	d_{bulk} (Å)	d_{exp} (Å)	Dd/d_{bulk}	FWHM (rad)	Ø (nm)	a (Å)
012	12.068	12.083	3.684	3.680	−0.001	0.041	34.647	8.229
104	16.579	16.579	2.700	2.699	-1.4×10^5	0.042	34.877	11.132
110	17.806	17.939	2.519	2.501	−0.007	0.042	34.778	3.537
113	20.428	20.466	2.207	2.203	−0.002	0.042	35.248	7.308
202	21.759	22.112	2.078	2.047	−0.015	0.042	35.688	5.788
024	24.690	24.766	1.841	1.839	−0.001	0.043	35.622	8.223
116	27.046	27.088	1.694	1.691	−0.002	0.043	35.955	10.427
122	28.665	28.826	1.603	1.598	−0.004	0.045	35.398	4.792
300	31.996	31.323	1.454	1.482	0.019	0.044	36.929	4.445
125	33.014	32.222	1.414	1.445	0.022	0.042	38.659	7.913
208	34.801	34.544	1.349	1.359	0.007	0.043	39.043	11.203
1010	35.969	35.799	1.312	1.317	0.004	0.045	37.909	13.236
220	37.715	37.671	1.259	1.261	0.001	0.045	39.360	3.565
223	39.380	39.611	1.214	1.208	−0.005	0.041	44.237	4.981
210	41.469	41.116	1.163	1.171	0.007	0.042	43.945	11.946
134	42.458	42.042	1.141	1.150	0.008	0.045	41.511	5.865
226	44.271	44.372	1.104	1.102	−0.002	0.044	44.629	7.307

List of Abbreviations, Symbols and Constants

SS	Stainless steel
η	Selectivity
FTIR	Fourier Transform Infrared
UV-vis-NIR	Ultraviolet-Visible-Near infrared
T	Absolute temperature
a	Lattice Constance
λ	Wavelength
(α)	Absorptance
(ε)	Emittance
a_{exp}	Experiment results
a_{bulk}	Results from database
d	inter-planar distances
Dd	Change in inter-planar distance
(R_{λ})	Total reflectance
AFM	Atomic Force Microscopy
EDS	Energy Dispersive Spectroscopy
XRD	X-ray Diffraction
SEM	Scanning Electron Microscopy

References

1. Simo, A.; Mwakikunga, B.; Sone, B.; Julies, B.; Madjoe, R.; Maaza, M. VO_2 nanostructures based chemiresistors for low power energy consumption hydrogen sensing. *Int. J. Hydrogen Energy* **2014**, *39*, 8147–8157. [CrossRef]
2. Sani, E.; Mercatelli, L.; Sans, J.-L.; Silvestroni, L.; Sciti, D. Porous and dense hafnium and zirconium ultra-high temperature ceramics for solar receivers. *Opt. Mater.* **2013**, *36*, 163–168. [CrossRef]
3. Abdullahi, S.A.; Akoba, R.; Khamlich, S.; Halindintwali, S.; Nuru, Z.; Maaza, M. Hydrothermal surface treatment of 434-L stainless-steel for spectra solar absorber application. *Infrared Phys. Technol.* **2021**, *117*, 103848. [CrossRef]
4. Qiu, X.L.; Gao, X.H.; He, C.Y.; Liu, G. Enhanced Thermal Stability of the TiB_2–ZrB_2 Composite Ceramic Based High Temperature Spectrally Selective Absorber Coatings: Optical Properties, Failure Analysis and Chromaticity Investigation. *Opt. Mater.* **2020**, *100*, 109666. [CrossRef]
5. Pang, X.; Zhou, F.; Li, B.; Jiang, J.; Zhou, J. Optical Thermostability and Weatherability of TiN/TiC-Ni/Mo Cermet-Based Spectral Selective Absorbing Coating by Laser Cladding. *Opt. Mater.* **2021**, *117*, 111195. [CrossRef]
6. Zhang, X.; Wang, X.; Zhang, X.; Li, Y.; Cheng, X. Effect of Multilayered CoO-$CoAl_2O_4$ Films on Improving Solar Absorptance of Co-WC Solar Selective Absorbing Coatings. *Vacuum* **2018**, *155*, 185–192. [CrossRef]
7. Gao, X.-H.; Wang, C.-B.; Guo, Z.-M.; Geng, Q.-F.; Theiss, W.; Liu, G. Structure, optical properties and thermal stability of Al_2O_3-WC nanocomposite ceramic spectrally selective solar absorbers. *Opt. Mater.* **2016**, *58*, 219–225. [CrossRef]

8. Liu, H.D.; Fu, T.R.; Duan, M.H.; Wan, Q.; Luo, C.; Chen, Y.M.; Fu, D.J.; Ren, F.; Li, Q.Y.; Cheng, X.D.; et al. Structure and thermal stability of spectrally selective absorber based on AlCrON coating for solar-thermal conversion applications. *Sol. Energy Mater. Sol. Cells* **2016**, *157*, 108–116. [CrossRef]
9. Yang, Z.; Tan, S.; Yang, J.; Li, Y.; Yang, X.; Deng, J. Study on the solar selectivity and air thermal stability of cobalt–nickel–iron oxide coating fabricated by spraying method. *Opt. Mater.* **2021**, *111*, 110573. [CrossRef]
10. Kaluža, L.; Šurca-Vuk, A.; Orel, B.; Dražič, G.; Pelicon, P. Structural and IR Spectroscopic Analysis of Sol-Gel Processed $CuFeMnO_4$ Spinel and $CuFeMnO_4$/Silica Films for Solar Absorbers. *J. Sol-Gel Sci. Technol.* **2001**, *20*, 61–83. [CrossRef]
11. Orel, Z.C. Characterisation of high-temperature-resistant spectrally selective paints for solar absorbers. *Sol. Energy Mater. Sol. Cells* **1999**, *57*, 291–301. [CrossRef]
12. Ning, Y.; Wang, J.; Sun, C.; Hao, Z.; Xiong, B.; Wang, L.; Han, Y.; Li, H.; Luo, Y. NiCrAlO/Al_2O_3 solar selective coating prepared by direct current magnetron sputtering and water boiling. *Sol. Energy Mater. Sol. Cells* **2021**, *219*, 110807. [CrossRef]
13. Pelenovich, V.; Liu, H.; Zeng, X.; Liu, Y.; Liu, K.; Yang, B. Graded solar selective absorbers deposited by non-equilibrium RF magnetron sputtering. *Sol. Energy Mater. Sol. Cells* **2021**, *230*, 111188. [CrossRef]
14. Wu, Y.; Hu, E.-T.; Cai, Q.-Y.; Wang, J.; Wang, Z.-Y.; Tu, H.-T.; Yu, K.-H.; Chen, L.-Y.; Wei, W. Enhanced thermal stability of the metal/dielectric multilayer solar selective absorber by an atomic-layer-deposited Al_2O_3 barrier layer. *Appl. Surf. Sci.* **2021**, *541*, 148678. [CrossRef]
15. Adiba; Pandey, V.; Munjal, S.; Ahmad, T. Structural and optical properties of sol gel synthesized NiO nanoparticles. *AIP Conf. Proc.* **2020**, *2270*, 110011. [CrossRef]
16. Liao, Q.; Zhang, P.; Yao, H.; Cheng, H.; Li, C.; Qu, L. Reduced Graphene Oxide–Based Spectrally Selective Absorber with an Extremely Low Thermal Emittance and High Solar Absorptance. *Adv. Sci.* **2020**, *7*, 1903125. [CrossRef]
17. Taha, F.; El Mahallawy, N.; Shoeib, M.A. A study of sol gel process parameters on CoCuMnOx selective coating characteristics. *Mater. Res. Express* **2020**, *7*, 026410. [CrossRef]
18. Testafamichael, T. Characterization of Selective Solar Absorbers. Ph.D. Thesis, Uppsala University, Uppsala, Sweden, 2000.
19. Zheng, L.; Zhou, F.; Zhou, Z.; Song, X.; Dong, G.; Wang, M.; Diao, X. Angular Solar Absorptance and Thermal Stability of Mo-SiO_2 Double Cermet Solar Selective Absorber Coating. *Sol. Energy* **2015**, *115*, 341–346. [CrossRef]
20. Yang, Y. The Study of Nanostructured Solar Selective Coatings. Ph.D. Thesis, University of York, Heslington, UK, 2012.
21. Lampert, C.M. Coatings for Enhanced Photothermal Energy Collection. *Sol. Energy Mater.* **1979**, *2*, 1–17. [CrossRef]
22. Alyousif, O.M. On the influence of thermo-mechanical process history on stress corrosion cracking of solution annealed type 304 stainless steel. *Nucl. Mater. Energy* **2021**, *29*, 101074. [CrossRef]
23. Nuru, Z.Y.; Perez, D.; Kaviyarasu, K.; Vantomme, A.; Maaza, M. Annealing effect on the optical properties and interdiffusion of MgO/Zr/MgO multilayered selective solar absorber coatings. *Sol. Energy* **2015**, *120*, 123–130. [CrossRef]
24. Zhao, S.S.; Gao, X.H.; Qiu, X.L.; Yu, D.M.; Tian, G.K. A Novel TiC-TiN Based Spectrally Selective Absorbing Coating: Structure, Optical Properties and Thermal Stability. *Infrared Phys. Technol.* **2020**, *110*, 103471. [CrossRef]
25. Trefon-Radziejewska, D.; Juszczyk, J.; Krzywiecki, M.; Hamaoui, G.; Horny, N.; Antoniow, J.-S.; Chirtoc, M. Thermal characterization of morphologically diverse copper phthalocyanine thin layers by scanning thermal microscopy. *Ultramicroscopy* **2022**, *233*, 113435. [CrossRef] [PubMed]
26. Kennedy, C.E. *Review of Mid- to High-Temperature Solar Selective Absorber Materials*; National Renewable Energy Lab.: Golden, CO, USA, 2002. [CrossRef]
27. Maniv, S.; Zangvil, A. Controlled texture of reactively rf-sputtered ZnO thin films. *J. Appl. Phys.* **1978**, *49*, 2787–2792. [CrossRef]
28. Akoba, R.; Abdullahi, S.A.; Sackey, J.; Nkosi, M.; Mothudi, B.M.; Nuru, Z.Y.; Maaza, M. Ultrasound-assisted wet chemical synthesis of texturized Mo/MoO_3 spectrally selective solar absorber coatings. *Thin Solid Films* **2021**, *735*, 138892. [CrossRef]
29. Tüzemen, E.; Kavak, H.; Esen, R. Influence of oxygen pressure of ZnO/glass substrate produced by pulsed filtered cathodic vacuum arc deposition. *Phys. B Condens. Matter* **2007**, *390*, 366–372. [CrossRef]
30. Kaźmierczak-Bałata, A.; Bodzenta, J.; Guziewicz, M. Microscopic investigations of morphology and thermal properties of ZnO thin films grown by atomic layer deposition method. *Ultramicroscopy* **2020**, *210*, 112923. [CrossRef]
31. Kareem, M.M.; Khodair, Z.T.; Mohammed, F.Y. Effect of Annealing Temperature on Structural, Morphological and Optical Properties of Zno Nanorod Thin Films Prepared by Hydrothermal Method. *J. Ovonic Res.* **2020**, *16*, 53–61.
32. Fang, Z.B.; Yan, Z.J.; Tan, Y.S.; Liu, X.Q.; Wang, Y. Influence of post-annealing treatment on the structure properties of ZnO films. *Appl. Surf. Sci.* **2005**, *241*, 303–308. [CrossRef]
33. Sackey, J.; Bashir, A.K.H.; Ameh, A.E.; Nkosi, M.; Kaonga, C.; Maaza, M. Date pits extracts assisted synthesis of magnesium oxides nanoparticles and its application towards the photocatalytic degradation of methylene blue. *J. King Saud Univ. Sci.* **2020**, *32*, 2767–2776. [CrossRef]
34. Dongol, M.; El-Denglawey, A.; El Sadek, M.S.A.; Yahia, I.S. Thermal annealing effect on the structural and the optical properties of Nano CdTe films. *Optik* **2015**, *126*, 1352–1357. [CrossRef]
35. Dongol, M.; El-Denglawey, A.; Elhady, A.; Abuelwafa, A. Structural properties of nano 5, 10, 15, 20-Tetraphenyl-21H,23H-porphine nickel (II) thin films. *Curr. Appl. Phys.* **2012**, *12*, 1334–1339. [CrossRef]
36. Dolzhenko, A.; Tikhonova, M.; Kaibyshev, R.; Belyakov, A. Microstructures and Mechanical Properties of Steels and Alloys Subjected to Large-Strain Cold-to-Warm Deformation. *Metals* **2022**, *12*, 454. [CrossRef]

37. Muchuweni, E.; Sathiaraj, T.; Nyakotyo, H. Synthesis and characterization of zinc oxide thin films for optoelectronic applications. *Heliyon* **2017**, *3*, e00285. [CrossRef]
38. Ghosh, R.; Basak, D.; Fujihara, S. Effect of substrate-induced strain on the structural, electrical, and optical properties of polycrystalline ZnO thin films. *J. Appl. Phys.* **2004**, *96*, 2689–2692. [CrossRef]
39. He, H.P.; Zhuge, F.; Ye, Z.Z.; Zhu, L.P.; Wang, F.Z.; Zhao, B.H.; Huang, J.Y. Strain and its effect on optical properties of Al-N codoped ZnO films. *J. Appl. Phys.* **2006**, *99*, 023503. [CrossRef]